Formation of plasmonic nanoparticle arrays – rules and recipes for an ordered growth

Karsten Fleischer[*,1] Oral Ualibek[1,2], Ruggero Verre[3], Igor V. Shvets[1],

[1] School of Physics, Trinity College Dublin, Dublin, Ireland
[2] National Laboratory Astana, Nazarbayev University, Astana, Kazakhstan
[3] Department of Applied Physics, Chalmers University of Technology, Göteborg, Sweden

Received XXXX, revised XXXX, accepted XXXX
Published online XXXX

Key words: Nano particle; plasmonic arrays; glancing angle deposition; reflectance anisotropy spectroscopy; RAS

[*] Corresponding author: e-mail fleisck@tcd.ie, Phone: +353-1-8963649

We review a self-assembled growth method for plasmonic nanoparticle arrays, based on glancing angle deposition. We produced ordered Ag, Au, and Cu nanoparticle arrays over large areas on different stepped oxide templates. Precise control over the final geometry can be difficult and we provide recipes to obtain macroscopically ordered structures.
We discuss the influence of the adsorbate diffusion length and facet termination on the shape and size distributions of metallic nanoparticle arrays and show that an increased ad-atom mobility leads to more regular arrays of spherical nanoparticles.
We also show how *in-situ* Reflectance Anisotropy Spectroscopy (RAS) can be used to extract indirect information on the nucleation and ripening the nanoparticles, as well as measure the plasmonic resonance.

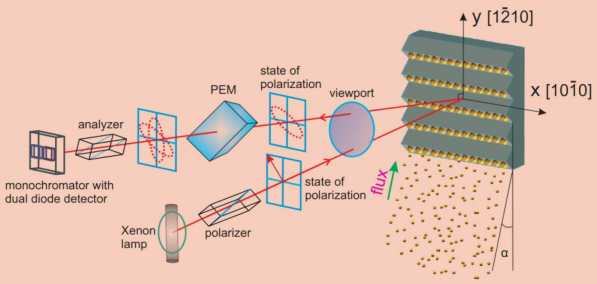

Schematics of the RAS setup used to *in-situ* monitor the growth of plasmonic nanoparticle arrays on stepped oxide templates.

1 Introduction Ordered arrays of small metallic nanoparticles (NPs) are promising material templates for new devices employing the physics of localised plasmon resonances [1,2]. When placed in close-proximity nanoparticle arrays act as a metasurface that have been shown potential for refractometric sensing [3–5], optoelectronic management [6,7] and for enhancing the solar cell efficiency [8,9]. Chemically synthesized and self-assembled methods have been shown tremendous progress in the last few years, providing unprecendented control over the shape and the dimensions of plasmonic nanoparticles [10–13]. Equally, it has been shown that the precise control over the nanoparticle position on a substrate is of crucial importance to tune the optical properties [14, 15] and enhance the electric fields in the gap region [16, 17]. Such control often requires slow, non scalable techniques such as electron beam lithography (EBL). While EBL grown arrays are highly customisable, scaling issues prevent the use in high volume production for low cost substrates employing plasmonic NPs. Such substrates are also desired for enhancing the signal in molecular spectroscopy, such as surface enhanced Raman spectroscopy (SERS), where molecules are placed in the localised in-

Table 1 Summary of template preparation conditions and step periodicity (L_y) for the different oxide samples used

	Al_2O_3	$SrTiO_3$	MgO
Terrace plane	(0001)	(001)	(001)
Off-cut	6°	3°	4°
T_{anneal}	1550-1700 K	1600 K	1550 K
Anneal time	15h	3h	3h
L_y	80-120 nm	120 nm	100 nm
Facet angle	42°	45°	10°
Facet plane	$(1\bar{2}16)$	(011)	(016)

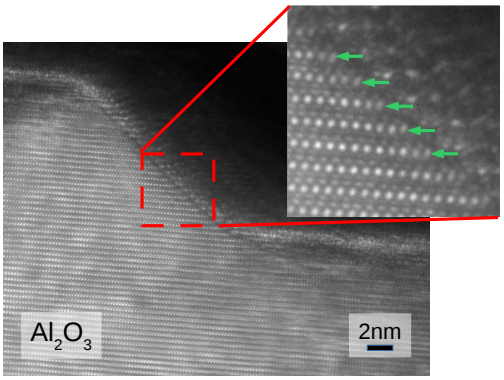

Figure 1 TEM image of an Al_2O_3 template. The presence of oxygen sites in the facet termination is marked by green arrows.

tense electric field regions to enhance their Raman signal [18–20, 17].

Previously we have shown that by glancing angle deposition (GLAD) of metals onto stepped oxide surfaces one can form well defined one-dimensional arrays of closely spaced, interacting metallic NPs [21–26]. In contrast to other methods, GLAD grown arrays provide the required tunability in size and NP spacing using a scalable technique. GLAD grown samples have already shown promise as SERS substrates on par with other methods to produce SERS substrate based on arrays of plasmonic NPs [27, 28].

The plasmonic resonance position of GLAD grown, ordered arrays depends on the polarisation of the incident light, leading to a strong optical anisotropy (birefringence). This anisotropy can be measured *in-situ* during growth and can be quantitatively and qualitatively related to the shape, order and size of the NP-arrays [22–25]. Here, we discuss the effects of different parameters affecting the growth, i.e. substrate temperature, periodicity, substrate material and evaporated metal. We will focus on the influence of the diffusion length of the adsorbate species on the final shape and size distribution of the NP arrays and prove how this affects the final order of the structure. Differences between GLAD and deposition on flat templates will also be discussed. We finally provide a "user guideline", with the parameters which should be used to achieve the best array order when employing the GLAD method.

2 Experiment Metal NP arrays have been prepared by glancing angle deposition on three different oxides. Vicinal, single sided polished, single crystal α-Al_2O_3(0001), $SrTiO_3$(001), and MgO(001) samples [MTI K.J group, USA] have been annealed in air at high temperatures to create stepped templates. In order to prepare templates with comparable step periodicity the annealing temperature, anneal time, as well as the off-cut angle between samples were all varied. Prior annealing in a tube furnace, samples were treated in an ultrasonic bath using acetone, methanol and high purity isopropanol. Further details on the dependence of the final template structure on annealing conditions has been previously published [29–31]. The anneal conditions and properties of templates used in this study are summarised in Table 1. The templates were loaded into a ultra high vacuum chamber and different metals were deposited selectively on the facets by tilting the sample to α=6°. The metal flux was kept constant at $\approx$2.5 Åmin^{-1}. The RAS spectra were taken *in-situ* at intervals during growth using a home-built system following the two polariser design of Aspnes *et.al.* [32]. The geometry is outlined in the title figure.

3 Nanoparticle nucleation Following the pioneering work of Venables *et.al.* the nucleation of metallic nanoparticles on flat substrates is governed by three distinct processes; the metal adsorption and desorption, adsorbate diffusion and metal-metal cluster formation. These processes are governed by the characteristic energy barriers for adsorbate desorption (E_a), adsorbate diffusion (hopping barrier, E_d), and finally the binding energy of a metal binary cluster (E_b) [33].

The value and differences between these energies determines the number density of nucleation centres and hence the final nanoparticle density (n_d). The model was originally formulated for the growth of metal clusters on metal halides, however, it has since then successfully applied to many nucleation processes and careful analysis of the number density, as function of growth temperature and ad-atom flux, can determine values for E_a, E_d, and E_b [33]. For most nucleation processes the difference between the diffusion barrier and desorption barrier ($\Delta E = E_a - E_d$) is the most important parameter as it affects the probability of an adsorbed atom leaving the surface, or diffusing over it. Phenomenologically if ΔE is large ($E_a > E_d$) the adsorbate sticks to the surface but easily moves on it leading to large isolated particles. If ΔE is small ($E_a \approx E_d$) it is equally likely that the adsorbate desorbs as diffusing on the surface. A large number of small particles is then expected. If ΔE is negative ($E_a < E_d$) an adsorbed species is more likely to leave the surface rather than diffusing on it, leading to homogeneous, closed films. In order to achieve a high density, closely spaced NPs a sit-

uation were $E_a \approx E_d$ and hence ΔE small is the optimum case.

For metal adsorption on oxide surfaces in particular, the nucleation density however can be dominated by the defect density of the surface, in particular cation vacancies can act as nucleation sites and significantly increase the initial cluster densities [34]. DFT calculations on metal adsorption on Al_2O_3 in particular have shown significantly higher adsorption energies and hopping barriers on an oxygen terminated surface compared to an aluminium terminated surface [35]. As shown in Fig. 1 the facet used in our glancing angle deposition consists of alternating oxygen and cation termination. We hence expect a much smaller diffusion length and higher nucleation density than in the case of deposition on metal terminated, flat facets.

After the initial nucleation the growth mode of the metal is determined by the differences in the surface free energies of the oxide $\gamma_{v,ox}$, the metal $\gamma_{v,m}$ and the interface free energy $\gamma_{ox/m}$. 3D growth occurs if $\gamma_{ox/m} > \gamma_{v,ox} + \gamma_{v,m}$ as the total energy is minimised if the least amount of oxide surface is covered [34]. This is typically the case for metals deposited on oxide surfaces (non wetting).

The shape of the grown nanoparticle is also governed by principles of energy minimisation and surface diffusion, i.e. the values of $\gamma_{v,ox}$, $\gamma_{v,m}$ and $\gamma_{ox/m}$ determine the nanoparticle contact angle. The size dependence of $\gamma_{v,m}$ and the surface diffusion (which governed by E_d) also affect the NP growth and shape. In particular Ostwald ripening can lead to the preference of larger NPs to grow, consuming smaller neighbouring NPs. The latter can lead to lower NP densities than expected by the simple nucleation theory alone [34].

Understanding the exact nucleation of a given metal on an oxide requires a careful analysis of size and number density of the NPs at different stages of the growth, temperatures, and growth rates to assess the relevant energies. In the case of the NPs grown by GLAD the situation is even more complex, as the deposition rate is effectively altered by the step height H_s and depostion angle α, as well as the ad-atom flux from the source. In addition, the facet termination and roughness are not well known, compared to flat oxide substrates, making it difficult to assess if the initial nucleation is kinetically limited, or dominated by defects.

Despite these complications, reported kinetic Monte Carlo simulations for Ag deposition on stepped SiO_2 revealed strong similarities to the nucleation principles from flat surfaces [36]. It was demonstrated that a small $\Delta E = E_a - E_d$ leads to larger, more isolated NPs, while values above 0.1eV lead to continuous rows of small NPs. We will show in the following that *in-situ* RAS measurements allow for an evaluation of ΔE and that the diffusion kinetics can be used to alter the order and shape of GLAD grown NP arrays.

4 Influence of temperature: Ag/Al_2O_3 In order to assess if the nucleation process of the NPs on stepped oxide templates can be described as a diffusion limited process we have investigated the temperature dependence for Ag NPs on Al_2O_3. On Al_2O_3 we achieve the best template quality, with regular faceted steps and atomically flat terraces [29]. Silver was chosen as adsorbate, as the RAS response of the NP-arrays is very well understood and not just the dipolar resonance, but also quadrupolar resonances can be measured as all plasmonic features are below the interband transitions of Ag [25,37,38].

The plasmonic response of linear arrays of metallic NPs is inherently anisotropic, as light polarised along and perpendicular to the array axis interacts differently. In the case of polarisation along the array the NPs are close together, leading to a strong interaction. For light polarised perpendicular the row spacing determines the inter particle interaction, which is much weaker than in the first case. Hence the reflectivity of the samples differs for light polarised along (R_x) and perpendicular (R_y) to the template steps. RAS measures the normalised difference in these two quantities ($2\frac{R_x - R_y}{R_x + R_y}$). Consequently a positive peak is seen in the energy range of the strongly interacting dipolar resonance ($R_x > R_y$), while a smaller negative peak is seen at higher frequencies, close to the resonance for non interacting NPs ($R_x < R_y$). The actual energetic position of these dipolar resonance depends on a variety of parameters such as size, spacing, material and shape and has been previously discussed in great detail [22–25,39]. In addition to this dipolar signature higher order structure, mainly a quadrupolar resonance can be seen at higher energies. The latter is more closely related to the contact angle of the MPs to the substrate and has been previously studied using numerical simulations [25].

Figure 2 shows the *in-situ* RAS spectra and SEM images of the final NP-arrays after exposure for different substrate temperatures. Even at a first glance the NPs look more irregular when grown at room temperature if compared to those grown at 470 K, leading to a significantly broader plasmonic resonance as seen in the RAS spectra. To quantify these changes NP size statistics have been extracted from the SEM images, as well as characteristic RAS features have been quantified at each growth step. These quantities are the amplitude of the dipolar resonance A, the intensity of the quadrupolar feature I_{QP}, the FWHM of the dipolar x-resonance Γ, the energetic position of the x-resonance E_x, and the rate of the energetic shift of the latter during the ripening process after initial nucleation ($\Delta\omega_0 = \frac{\Delta E_x}{\Delta t}$).

Figure 3 illustrates the correlation of the quantities extracted from the RAS spectra to certain morphological aspects of the NP arrays. Previously, we have investigated the position and width of the plasmonic resonance using dipolar analytical models and have identified the origin of the quadrupolar resonances [22–25,39]. For a given NP material the position of the x-resonance ω_x depends not only

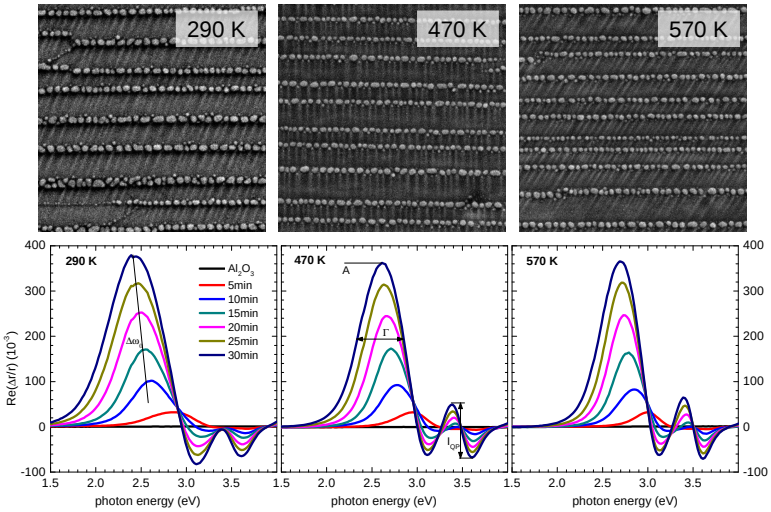

T	290K	370K	470K	570K
D_x (nm)	25±10	25±11	21±7	20±6
D_y (nm)	21±6	21±7	19±5	18±5
D_z (nm)	9	9	10	10.5
D_x/D_y	1.21	1.19	1.13	1.09
L_x (nm)	26±11	28±13	24±10	22±10
L_y (nm)	80±15	80±15	80±15	80±15
d_x (nm)	1±1	3±2	3±2	2±1
n_d (μm^{-2})	490	450	520	550
Quantities from RAS spectra:				
I_{QP}/A	0.17	0.26	0.32	0.37
A (10^{-3})	380	390	360	365
$\Delta\omega_0$ (meV/min)	-9	-7	-6	-5
ω_x (eV)	2.4	2.5	2.6	2.7
Γ (eV)	0.68	0.68	0.55	0.48

Figure 2 Comparison of Ag NPs grown at different temperatures. The NP arrays grown at elevated temperatures are more ordered with more spherical, larger NPs due to the increased diffusion length of Ag. The top row shows SEM images (field of view 0.75µm×0.75µm) and the extracted average NP dimensions: D_x length of the NP, D_y width of the NP, D_z height of the NP, D_x/D_y ellipticity, L_x, L_y average centre to centre distance in x and y, d_x average gap between NPs, and n_d the nanoparticle density. The average NP height (D_z) has been estimated using the known deposited total Ag volume and extracted D_x and D_y values assuming a hemispherical shape. The bottom row shows corresponding RAS spectra for these samples. The increase in order leads to a sharpening of the plasmonic resonance. The increased average gap size leads to a blue shift of the resonance and the quadrupolar resonance in the UV is more pronounced. Several quantities have been extracted from the RAS spectra as indicated in the lower panel. These quantities are the amplitude of the dipolar resonance A, the intensity of the quadrupolar feature I_{QP}, the FWHM of the dipolar x-resonance Γ, and the rate of the energetic shift in the x-resonance position $\Delta\omega_0 = \frac{\Delta\omega_x}{\Delta t}$. The tabulated values in the Figure refer to the final spectra prior ambient exposure and transfer to the SEM.

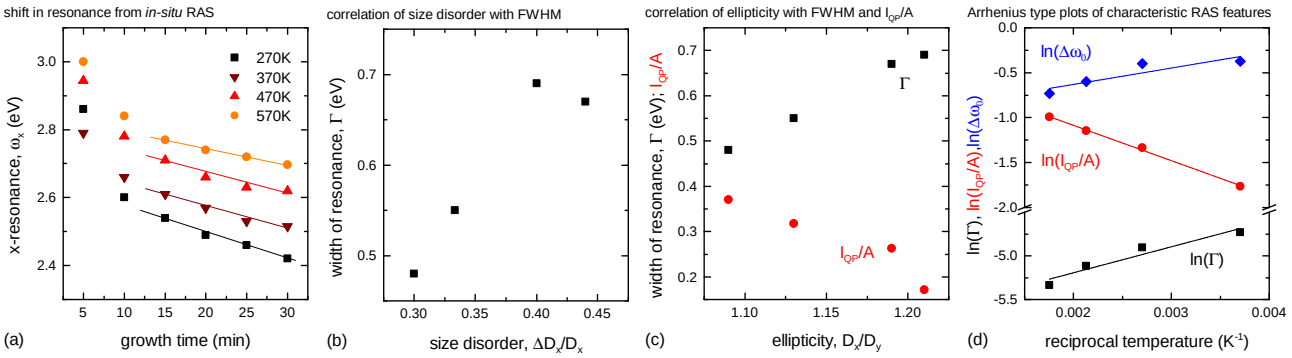

Figure 3 Analysis of the temperature dependence of key RAS spectral parameter extracted from *in-situ* measurements. (a) illustrates the rate of change in the x-resonance $\Delta\omega_0$ for all analysed samples. (b) and (c) demonstrate the correlation of the width of the plasmonic peak Γ and the amplitude ratio of quadrupolar to dipolar resonance I_{QP}/A to morphological parameter extracted from the SEM images. (d) shows the temperature dependence of these quantities in an Arrhenius type plot, allowing for the quantification of the underlying activation energy for the ordering process (ΔE).

on the NP volume and average gap size between the nanoparticles but also on the size distribution [24] and ellipticity [23]. Consequently changing the growth temperature does not alter just one of these parameters; some of them are interdependent. In particular the width of the plasmonic resonance is not just linked to the size distribution (Fig. 3(b)), but also in the irregularities of the NPs' shape. The irregular shape is an apparent average ellipticity of the NPs. The quadrupolar resonance, which is very prominent in *in-situ* measurements, is particularly sensitive to the shape of the NPs and a strong correlation to the average ellipticity from SEM images can be seen (Fig. 3(c)).

Apart from the correlation to the NP morphology, the analysis of the RAS spectra can also be used to assess the underlying activation energy, ΔE, of the ordering process. Figure 3(d) shows Arrhenius type plots of the investigated

quantities $\Delta\omega_x$, Γ, and I_{QP}/A resulting in a ΔE of 15, 25, and 34 meV, respectively. If only data for elevated growth temperatures (370-570 K) are considered all independently determined quantities result in a similar ΔE of 34±5 meV. As outlined previously the relevant energy scale for diffusion is the difference in the barriers for desorption and adsorbate site hopping $\Delta E = E_a - E_d$. The experimentally determined value of ΔE of 34±5 meV is comparable to one found by analysing glancing angle deposition of Ag on rippled SiO_2 surfaces [36]. Using kinetic Monte Carlo simulations, outlined previously by Numazawa *et. al.*, a characteristic energy ΔE of around 45 meV was required to describe the shape and distribution of GLAD grown NPs on rippled SiO_2 templates. The slightly lower value found here for Ag on stepped Al_2O_3 can explain why the overall order of the arrays is significantly better compared to similar structures grown on rippled SiO_2.

The GLAD grown NP arrays have a small gap distance and high density of NPs within the row compared to random NP distributions grown on flat oxide substrates. The nucleation discussion done here already provides an indication on the mechanism. The number density of the NPs is not affected by the growth temperature (see statistics from SEM in Fig. 2). As outlined by Venables *et. al.* [33] for generic nucleation processes, and by Campbell *et. al.* [34] for metals on oxide surfaces specifically, the number density should decrease with increasing temperature due to an increased mobility of adsorbed metal species. Clearly this is not the case for the GLAD grown NPs on faceted oxide templates. First of all due to the deposition geometry the arrival rate of ad-atoms is restricted to the stepped facet, which leads already to a locally high ad-atom flux compared to the same amount of metal volume deposited on a flat terrace. Even at low metal coverages we hence already operate in a high flux regime leading to a higher local NP density. Secondly the microstructure of the facets is less ordered than the low index surfaces typically used. We therefore expect a higher defect density than for flat oxide surfaces, in the sense that there are more surface oxygen sites with stronger bonds to the adsorbed metal (see Fig. 1). As a consequence the nucleation density is no longer comparable to flat substrates, but significantly higher. Due to limitations in our experimental setup, the investigated temperature range is quite small, however if we compare our results to Ag NPs grown on flat Al_2O_3 a change in number density of one order would be expected for the change from room temperature to 570 K for a diffusion limited nucleation [40].

As the overall nucleation density is not diffusion limited, the remaining temperature dependence is solely related to the dynamic exchange of metal ad-atoms between adjacent NPs during the growth and ripening process. Phenomenologically we observe more spherical NPs with narrower size distribution at elevated temperatures. On flat surfaces the ripening stage is typically governed by the size and temperature dependence of the metal surface free energy $\gamma_{v,m}$ and can frequently lead to a consumption of smaller particles by neighbouring larger NPs (Ostwald ripening). Our measurements show, that while there are distinct shape changes from more elliptical NPs to truncated spheres at higher temperatures (see origin of more pronounced quadrupolar resonance [25]), we do not observe significantly larger NPs at elevated temperatures. Again we can attribute this due to the peculiarities of GLAD grown NP arrays; NPs are confined to the step factet and material exchange is only possible over the nearest neighbours. There is an inherent size confinement by the actual step width.

5 Influence of substrate: Ag on Al_2O_3, $SrTiO_3$, and MgO The dynamics of the ad-atom diffusion is controlled by the energy barriers for adsorbate desorption E_a and adsorbate diffusion E_d. Both values are dependent on the atomic termination of the investigated substrate. DFT calculations on different $Al_2O_3(0001)$ terminations have shown that binding energies can vary significantly [41]. Unfortunately, there are no calculations on the $(1\bar{2}16)$ facet used for deposition in our case. In order to illustrate the significance of the surface termination we have investigated deposition on different oxide surfaces.

Figure 4 shows SEM images and *in-situ* RAS spectra for the growth of Ag on Al_2O_3, $SrTiO_3$ and MgO for comparable terrace widths. GLAD is a deposition method mainly dependent on the deposition geometry itself, and the SEM images confirm this: NP arrays were formed regardless of the substrate used. However, as shown in Table 1, the use of a different oxide not only alters the surface termination but also the geometry of the steps and, due to the deposition geometry, also the ad-atom flux. For this reason, we cannot obtain quantitative information on the growth characteristics and surface diffusion directly. We can however simply and more importantly assess the feasibility of each substrate for the formation of ordered NP arrays. Distinct differences in NP shape, size, size distributions are found upon changes of the substrate.

If we compare the data for Al_2O_3 and $SrTiO_3$ it is apparent, that for the growth on Al_2O_3 the terraces are void of smaller NPs. On $SrTiO_3$ terrace nucleation is more prominent, leading to significantly lower RAS amplitudes while the shape and spectral shape of the plasmonic resonance are very similar, with slightly smaller NPs in case of the $SrTiO_3$ substrate, due to a shorter step width and therefore smaller amount of Ag deposited in the same time. While the choice of equal deposition angle α ensures that the ad-atom flux is similar between growth on Al_2O_3 and $SrTiO_3$ due to their similar facet angle, the smaller off-cut angle in case of $SrTiO_3$ leads to a significant amount of Ag being deposited on the terrace as evident by on terrace nucleation and a reduction in RAS amplitude due to the increased isotropic reflectance of the terrace.

In the case of MgO the deposition angle was therefore adjusted to 4°, equivalent to the off-cut angle. Terrace nu-

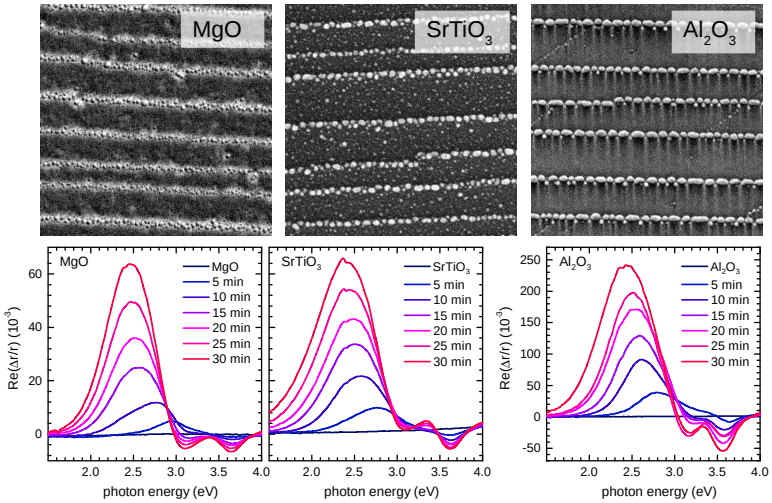

Substrate	MgO	$SrTiO_3$	Al_2O_3
D_x (nm)	8±6	18±7	21±6
D_y (nm)	7±5	15±6	18±4
D_z (nm)	8	11	12
D_x/D_y	1.14	1.20	1.16
L_x (nm)	10±6	22±9	24±7
L_y (nm)	100±26	120±23	120±23
d_x (nm)	2±1	4±2	3±2
n_d (μm^{-2})	1400±400	460±130	290±90
Quantities from RAS spectra:			
I_{QP}/A	0.088	0.16	0.17
A (10^{-3})	63	65	240
$\Delta\omega_0$ (meV/min)	-6.2	-6.8	-6
ω_x (eV)	2.46	2.40	2.43
Γ (eV)	0.68	0.80	0.74

Figure 4 Comparison of Ag NPs grown on Al_2O_3, $SrTiO_3$ and MgO stepped substrates. The terrace width and step height is comparable between substrates. The apparent difference in NP size and order as seen in SEM images (field of view 0.75µm×0.75µm) is caused by a combination in step width, l_s and substrate defect density. The bottom row shows corresponding RAS spectra for these samples, illustrating the impact of the microstructure on the plasmonic resonance of the NP array.

cleation is hence reduced. However due to the wider step width in case of MgO, caused by the reduced facet angle, the total step area is increased and the total flux per surface area on the step edge is reduced by factor of 0.67 due to the change in deposition angle and another factor of 0.25 due to the shallower facet angle. Hence the 30 min deposition on MgO is more equivalent to a 5 min deposition on Al_2O_3, leading to much smaller NPs, a lower RAS amplitude, and changed RAS line shape.

These results already highlight the limitations of the *in-situ* RAS measurements, as the RAS amplitude of the measurements on $SrTiO_3$ and MgO are similar but the underlying NP size is hugely different (see Fig. 4). This is a natural consequence of the nature of the measurement: one can only follow the peak position and intensity using *in-situ* RAS, but these are in turn affected by multiple, intercorrelated parameters. Only indirect and qualitative information can hence be obtained. In cases where the NP size and shape are similar between NPs e.g. if formed on Al_2O_3 and $SrTiO_3$, the RAS amplitude can then be hugely different if there is unwanted deposition on the terrace, as RAS measures only the relative anisotropy between orthogonal directions. As some parameters cannot be freely chosen such as the facet angle, as its an inherent substrate property a more comprehensive study would be required to decouple the influence of the geometric factors from diffusion processes. So far this study has only be carried out for the case of Ag growth on Al_2O_3 in the previous section as it is the substrate which presents the most ordered NP arrays.

It should be noted though that the geometric differences between different substrates offer a way to additionally tune the local morphology of the plasmonic nanoparticles. As seen in Fig. 4 the resonance of all samples is ≈2.4 eV, while the NP density, size, and separation hugely varies. This offers even further ways to control the resonance frequency, while retaining freedom to change other parameters to optimise the array for applications e.g. increasing the NP density for better signal to noise in SERS.

Similar to the case for Ag on Al_2O_3, GLAD deposited NPs on MgO and $SrTiO_3$ show higher nucleation densities and better size homogeneity then in studies on corresponding flat surfaces [42,43]. Again this is a result of the high defect densities and the confinement of the adatom flux to small areas of the substrate surface. Assuming similar defect densities in the case of MgO we expect a higher NP density by a factor of 4, this is due to the wider steps exposing a larger surface area to the ad-atom flux if compared to $SrTiO_3$ or Al_2O_3 substrates. The density extracted from the SEM images is roughly in line with this further confirming a defect limited nucleation, as for diffusion limited nucleation this would manifest as an apparent lower flux which would result in a lower NP density. Further experiments have to show if this increased density can be maintained for higher coverages – or if in the later stages of growth increased Ostwald-ripening will significantly reduce the NP density.

6 Influence of adsorbate metal: Ag,Au, and Cu on Al_2O_3 As the deposition method for the self-organised NP-arrays is based on geometric shadowing, it is also broadly independent on the deposited material. As seen above, the initial nucleation density is governed by the defect density of the substrate and the step facet in particular. The growth and ripening process of the NPs is governed by inter particle material exchange though and is affected by the ad-atom diffusion. The latter is dependent on the evaporated metal species as binding energies of different metals can differ on the same substrate. DFT calculations,

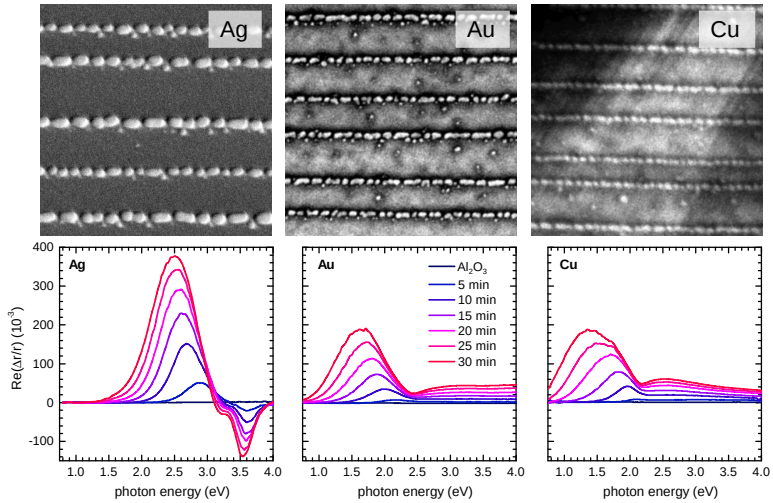

Adsorbate	Ag	Au	Cu
D_x (nm)	29±11	22±3	24±5
D_y (nm)	20±8	14±2	16±3
D_z (nm)	12	12	12
D_x/D_y	1.45	1.57	1.5
L_x (nm)	35±13	25±10	27±7
L_y (nm)	100±29	100±21	100±21
d_x (nm)	6±3	3±2	3±2
N (μm^{-2})	340±100	420±100	390±100
Quantities from RAS spectra:			
I_{QP}/A	0.28	-	-
A (10^{-3})	380	190	188
$\Delta\omega_0$ (meV/min)	-7.6	-11	-23
ω_x (eV)	2.48	1.64	1.36
Γ (eV)	0.75	0.86	1.05

Figure 5 Comparison of Ag, Au, and Cu NPs arrays grown on Al_2O_3. The geometry of the NPs is very similar for all metal species as seen in the SEM images (field of view 0.5µm×0.5µm) and extracted average NP dimension. In contrast to the examples shown above the position of the resonance as seen in the RAS spectra in the bottom row is dominated by the differences in the metals dielectric function, rather then changes in NP size and geometry

specifically for Cu, Au, and Ag have shown variations in E_a for an Al-terminated surface from 0.6 up to 1.1 eV with copper interacting more strongly [35].

We therefore compare the growth of Au, Cu and Ag NP arrays on Al_2O_3 stepped surfaces. Figure 6 illustrates that only small changes in NP morphology were found, while RAS spectra and the position of the plasmonic resonance differ due to significant changes in the metal dielectric function. In agreement with the calculated lower binding energy for silver ad-atoms and standard nucleation theory, Ag NPs are found to be larger, with lower total NP density and larger NP gaps. The observed morphological differences between Au and Cu NPs are smaller and no clear trend is observed. Again this is adds to the finding that the NP density is limited by defect nucleation rather than diffusion limited nucleation as already seen in the temperature dependent analysis for Ag on Al_2O_3.

Changing the metal dramatically changes the plasmon resonance frequency. The energetic position changes more dramatically with the NP size as seen in an increased value for $\Delta\omega_0$ for Au and even more for Cu. For precise control of the resonance frequency the *in-situ* measurements by RAS are even more helpful for these materials. The shape dependence of the quadrupolar resonance, which was given the clearest indication for diffusion limited NP ripening processes in the case of Ag on Al_2O_3, is absent however in the case of Au and Cu NPs. This is caused by the strong interband transitions above 2.4 eV and 1.8 eV for Au and Cu respectively, which dampens the signal of these resonances in RAS spectra.

7 Optimized recipes for ordered templates Based on the presented work on GLAD grown nanoparticle arrays we can formulate generic guidelines on achieving the best NP order:

Substrate: The study performed suggests that Al_2O_3 is the ideal candidate both in terms of regularity of the stepped surface after annealing, and in terms of improved regularity of the nanoparticle arrays and in optical anisotropy. MgO can be used if a higher NP density is of interest.

Deposition angle: A previous study demonstrated that for vicinal annealed templates the deposition angle should be chosen equal to the miscut angle. Higher angles lead to unwanted nucleation on the terraces, while lower angles lead to a broader NP size distribution due to an increased self-shadowing [24, 22].

Substrate temperature and flux: Whenever possible, the deposition should be performed at elevated high temperatures. The flux does not play a crucial role in the initial stages of deposition, as the growth is defect nucleation limited.

Template periodicity: The template periodicity affects the final NP dimensions and the plasmonic resonance position. This is dominated by the altered step height and the NP size confinement in y-direction

Deposition time: By using *in-situ* RAS one can measure the resonance position during the growth. Exact time and flux control is hence not any longer an issue. The deposition can be stopped in order to obtain resonances at chosen energies.

8 Summary During the self-organized formation of metallic nanoparticle arrays on stepped oxide templates the metal species diffusion length plays a role in the nucleation and ripening processes of the NPs. By varying the growth temperature for growth of Ag NPs on Al_2O_3 we

have demonstrated general trends that increasing diffusion length leads to more ordered, spherical and larger nanoparticles. By comparing growth on different substrates we have demonstrated the general applicability of the GLAD growth process, but that more systematic studies would be required to decouple changes caused by unavoidable differences in geometry from changes in diffusion processes on the varying oxide surfaces. These effects should be taken into account in designing such NP arrays for sensing applications, as the correct choice of substrate, metal and growth temperature can be used to minimise the average gap size, maximise overall coverage and at the same time maintain tunability of the resonance position. For the latter *in-situ* measurements of the plasmonic resonance by RAS has been shown to be a valuable tool in growth optimisation.

Acknowledgements This work was supported by SFI 06/IN.1/I01 and the INSPIRE programme under the Irish Governments PRTLI Cycle 4 (NDP 2007-2013). O. Ualibek acknowledges the support of the Government of Republic of Kazakhstan under Bolashak programme.

References

[1] U. Kreibig and M. Vollmer, Optical Properties of Metal Clusters (Springer, Berlin, 1957).
[2] V. Shalaev and S. Kawata, Nanophotonics with Surface Plasmons (Springer, Berlin, 2007).
[3] A. Dahlin, N. Wittenberg, F. Hook, and S. Oh, Nanophotonics **3** (2013).
[4] V. G. Kravets, F. Schedin, R. Jalil, L. Britnell, R. V. Gorbachev, D. Ansell, B. Thackray, K. S. Novoselov, A. K. Geim, A. V. Kabashin, and A. N. Grigorenko, Nat. Mat. **12** (2013).
[5] M. Svedendahl, R. Verre, and M. Käll, Light: Science & Applications **3**(11), e220 (2014).
[6] S. Maier, P. Kik, A. Atwater, and S. Meltzer, Nat. Mater. **2**(229) (2003).
[7] M. Abb, P. Albella, J. Aizpurua, and O. L. Muskens, Nano Lett. **11**(6), 2457–2463 (2011), PMID: 21542564.
[8] H. A. Atwater and A. Polman, Nat. Mater. **9**(3), 205–213 (2010).
[9] S. C. Warren and E. Thimsen, Energy Environ. Sci. **5**, 5133–5146 (2012).
[10] S. Barbosa, A. Agrawal, L. Rodrguez-Lorenzo, I. Pastoriza-Santos, R. A. Alvarez-Puebla, A. Kornowski, H. Weller, and L. M. Liz-Marzn, Langmuir **26**(18), 14943–14950 (2010), PMID: 20804155.
[11] J. M. Romo-Herrera, R. A. Alvarez-Puebla, and L. M. Liz-Marzan, Nanoscale **3**, 1304–1315 (2011).
[12] H. Chen, L. Shao, Q. Li, and J. Wang, Chem. Soc. Rev. **42**, 2679–2724 (2013).
[13] A. Sánchez-Iglesias, P. Aldeanueva-Potel, W. Ni, J. Pérez-Juste, I. Pastoriza-Santos, R. A. Alvarez-Puebla, B. N. Mbenkum, and L. M. Liz-Marzán, Nano Today **5**(1), 21–27 (2010).
[14] A. G. Curto, G. Volpe, T. H. Taminiau, M. P. Kreuzer, R. Quidant, and N. F. van Hulst, Science **329**(5994), 930–933 (2010).
[15] R. Verre, Z. J. Yang, T. Shegai, and M. Kll, Nano Lett. **15**(3), 1952–1958 (2015), PMID: 25621936.
[16] T. V. Teperik, P. Nordlander, J. Aizpurua, and A. G. Borisov, Opt. Express **21**(22), 27306–27325 (2013).
[17] H. Lee, G. H. Kim, J. H. Lee, N. H. Kim, J. M. Nam, and Y. D. Suh, Nano Lett. **15**(7), 4628–4636 (2015), PMID: 26075353.
[18] C. E. Talley, J. B. Jackson, C. Oubre, N. K. Grady, C. W. Hollars, S. M. Lane, T. R. Huser, P. Nordlander, and N. J. Halas, Nano Lett. **5**(8), 1569–1574 (2005).
[19] E. C. Le Ru, E. Blackie, M. Meyer, and P. G. Etchegoin, The Journal of Physical Chemistry C **111**(37), 13794–13803 (2007).
[20] A. Hakonen, M. Svedendahl, R. Ogier, Z. J. Yang, K. Lodewijks, R. Verre, T. Shegai, P. O. Andersson, and M. Kall, Nanoscale **7**, 9405–9410 (2015).
[21] J. M. Flores-Camacho, L. D. Sun, N. Saucedo-Zeni, G. Weidlinger, M. Hohage, and P. Zeppenfeld, Phys. Rev. B **78**(Aug), 075416 (2008).
[22] R. Verre, K. Fleischer, R. G. S. Sofin, N. McAlinden, J. F. McGilp, and I. V. Shvets, Phys. Rev. B **83**(12), 125432–125440 (2011).
[23] R. Verre, K. Fleischer, O. Ualibek, and I. V. Shvets, Appl. Phys. Lett. **100**(3), 031102 (2012).
[24] R. Verre, K. Fleischer, J. F. McGilp, D. Fox, G. Behan, H. Zhang, and I. V. Shvets, Nanotechnology **23**(3), 035606 (2012).
[25] O. Ualibek, R. Verre, B. Bulfin, V. Usov, K. Fleischer, J. F. McGilp, and I. V. Shvets, Nanoscale **5**, 4923–4930 (2013).
[26] R. Verre, M. Modreanu, O. Ualibek, D. Fox, K. Fleischer, C. Smith, H. Zhang, M. Pemble, J. F. McGilp, and I. V. Shvets, Phys. Rev. B **87**(Jun), 235428 (2013).
[27] O. Ualibek, E. Razvani, R. Verre, K. Fleischer, B. Bulfin, O. Toktarbaiuly, G. S. Duesberg, and I. V. Shvets, too be published (2015).
[28] N. Pazos-Perez, W. Ni, A. Schweikart, R. A. Alvarez-Puebla, A. Fery, and L. M. Liz-Marzan, Chem. Sci. **1**, 174–178 (2010).
[29] R. Verre, R. Sofin, V. Usov, K. Fleischer, D. Fox, G. Behan, H. Zhang, and I. Shvets, Surf. Sci. **606**(23–24), 1815–1820 (2012).
[30] H. C. Wu, A. Syrlybekov, O. Mauit, A. Mouti, C. O. Coileáin, M. Abid, M. Abid, and I. V. Shvets, Appl. Phys. Lett. **105**(13), 132408 (2014).
[31] A. Syrlybekov, E. Arca, R. Verre, C. O. Coileain, R. Sofin, R. Ramos, O. Toktarbaiuly, A. Khalid, H. Zhang, and I. V. Shvets, too be published (2015).
[32] D. E. Aspnes and A. A. Studna, Phys. Rev. Lett. **54**(Apr), 1956–1959 (1985).
[33] J. Venables, G. Spiller, and M. Hanbucken, Reports on Progress in Physics **47**(4), 399 (1984).
[34] C. T. Campbell, Surf. Sci. Rep. **27**(1), 1–111 (1997).
[35] N. C. Hernández, J. Graciani, A. Márquez, and J. F. Sanz, Surf. Sci. **575**(1), 189–196 (2005).
[36] S. Numazawa, M. Ranjan, K. H. Heinig, S. Facsko, and R. Smith, J. Phys.: Condens. Matter **23**(22), 222203 (2011).
[37] F. Zhou, Z. Y. Li, Y. Liu, and Y. Xia, The Journal of Physical Chemistry C **112**(51), 20233–20240 (2008).

[38] C. P. Burrows and W. L. Barnes, Opt. Express **18**(3), 3187–3198 (2010).
[39] R. Verre, K. Fleischer, C. Smith, N. McAlinden, J. F. McGilp, and I. V. Shvets, Phys. Rev. B **84**(Aug), 085440 (2011).
[40] R. Lazzari and J. Jupille, Nanotechnology **23**(13), 135707 (2012).
[41] R. Meyer, Q. Ge, J. Lockemeyer, R. Yeates, M. Lemanski, D. Reinalda, and M. Neurock, Surf. Sci. **601**(1), 134–145 (2007).
[42] C. Revenant, G. Renaud, R. Lazzari, and J. Jupille, Nuclear Instruments and Methods in Physics Research Section B: Beam Interactions with Materials and Atoms **246**(1), 112–117 (2006).
[43] F. Silly and M. R. Castell, Appl. Phys. Lett. **87**(21), 213107–213107 (2005).